

Article

# Five-Band Tunable Terahertz Metamaterial Absorber Using Two Sets of Different-Sized Graphene-Based Copper-Coin-like Resonators

Jieru Wang, Xuefeng Qin, Qian Zhao, Guiyuan Duan and Ben-Xin Wang \* 

School of Science, Jiangnan University, Wuxi 214122, China

\* Correspondence: wangbenxin@jiangnan.edu.cn

**Abstract:** In this paper, a five-band metamaterial absorber with a tunable function in a terahertz band is proposed, which consists of a gold grounding layer, a polyimide dielectric layer, and a periodic patterned graphene layer. The patterned graphene layer is constructed from two sets of copper-coin-shaped structures of different sizes. The designed absorber achieves absorptions of 96.4%, 99.4%, 99.8%, 98.4%, and 99.9% at 4.62 THz, 7.29 THz, 7.70 THz, 8.19 THz, and 8.93 THz, respectively, with an average absorption intensity of 98.78%. The physical mechanism of this five-band absorber was explained by the impedance matching principle and electric field distribution. The absorption performance of the five-band absorber can be effectively tuned by changing the geometry of the patterned graphene array and the thickness of the dielectric layer. Given that the resonant frequency of the absorber varies in proportion to the Fermi level, by varying the Fermi level of the graphene hypersurface, we can achieve the continuous tuning of the absorption performance over a wide frequency range. The five-band absorber has a stable absorption performance over a wide incidence angle of 0–65°, and by combining the merits of high absorption, dynamic adjustability, and a large number of absorption peaks, the given absorber could have great potential for applications in nondestructive testing, imaging, communication, sensing, and detectors.

**Keywords:** terahertz metamaterials; graphene-based copper-coin-like resonator; multi-band absorption; tunable absorption properties



**Citation:** Wang, J.; Qin, X.; Zhao, Q.; Duan, G.; Wang, B.-X. Five-Band Tunable Terahertz Metamaterial Absorber Using Two Sets of Different-Sized Graphene-Based Copper-Coin-like Resonators. *Photonics* **2024**, *11*, 225. <https://doi.org/10.3390/photonics11030225>

Received: 18 January 2024  
Revised: 21 February 2024  
Accepted: 26 February 2024  
Published: 29 February 2024



**Copyright:** © 2024 by the authors. Licensee MDPI, Basel, Switzerland. This article is an open access article distributed under the terms and conditions of the Creative Commons Attribution (CC BY) license (<https://creativecommons.org/licenses/by/4.0/>).

## 1. Introduction

Terahertz (THz) is an electromagnetic wave with a frequency range from 0.1 THz to 10 THz [1]. Due to the special position of the terahertz band between the microwave and infrared bands of the electromagnetic spectrum, terahertz bands share the properties of electrons and photons. Consequently, terahertz exist vast applications in imaging technology [2], spectral resolution [3], and communication technology [4]. Metamaterials are artificially structured materials consisting of subwavelength arrays of periodically or non-periodically arranged resonant crystal cells [5], which are regarded as equivalent media, and the equivalent permittivity  $\epsilon(\omega)$  and equivalent permeability  $\mu(\omega)$  can be manipulated according to the actual needs to realize the absorption of electromagnetic waves of different frequencies [6]. It has bizarre properties beyond natural materials, including a negative refractive index [7,8], ultra-thin perfect absorption [9,10], an inverse Doppler effect [11,12], and so on. In view of the physical properties of metamaterials, in line with the current design needs for the miniaturization and integration of electronic components, a variety of metamaterial functional devices applicable to different scenarios has been widely proposed, which are of great significance for the research of stealth technology, perfect absorption [13], plasma-induced transparency [14,15], and sensors [16,17].

Among the above functional devices, metamaterial absorbers have received much attention for their advantages of small sizes, light weight, and high absorption. Landy et al. realized perfect absorption in the microwave band for the first time based on the resonant

structure of metal surfaces in 2008 [18]. With the continuous development of micro and nanotechnology, perfect absorption has been gradually introduced into visible, infrared, and terahertz bands [19–21]. Among them, perfect absorbers (PAs), which produce a strong response in the terahertz band, have become quite attractive in recent years [22,23]. To expand the potential applications of PAs, there is an urgent need for PAs with tunable performance or multi-band perfect absorbers. According to the number of resonant absorption peaks, multi-band metamaterial absorber devices can be categorized as dual-band absorbers, triple-band absorbers, quadruple-band absorbers, or even five-band absorbers. For example, Wen et al. developed a dual-band polarization-insensitive electromagnetic wave absorber by exploiting the LC resonance of metamaterials to produce a strong absorption point [24]. A three-band terahertz absorber utilizing three concentric square ring resonators was reported to achieve triple-frequency absorption with both high sensitivity and polarization insensitivity [25]. Fu et al. realized a multiwavelength absorber based on a metallic subwavelength structure using hexagonal filled nanoring–nanodisc composite arrays to introduce an asymmetric structure and realize new absorption functions [26]. However, the above proposed multi-band absorbers are usually based on metallic subwavelength structures, and once the original geometrical structure is determined, their optical properties are difficult to change, with the typical defect of a limited tuning range [27–29].

Graphene, as a two-dimensional nanomaterial, has excellent optical and electrical properties such as high carrier mobility, low loss, and an ultrafast optical response time [30–32]. When a bias voltage is added to the surface of graphene, the Fermi level of graphene varies with the external voltage, which results in the continuous regulation of conductivity over a wide frequency range [33–41]. Graphene has been widely used to construct tunable PAs, mainly including multi-band and broadband absorption. The realization of multi-band absorption performance is mainly classified into vertical stacked and coplanar types, which can bring about significant improvements in absorption performance by stacking multilayers of graphene, designing graphene gratings, and changing the periodic array pattern to increase the number of graphene resonators. For example, in 2019, Liu et al. proposed a dynamically and independently tunable absorber based on multilayered metal-graphene metamaterials, which can be arbitrarily tailored to dual-band or even multi-band absorption efficacy by stacking multiple metal–graphene layers [41–49]. However, the vertical stacking type often brings more complicated structures, and various multilayer designs lead to thicker structure dimensions, which makes practical production difficult [50–52]. Most of the absorbers also have limitations, such as a low number of absorption peaks, poor absorption quality, and insensitivity of polarization, so it is still feasible to explore a simple structure of a high-quality multi-band absorber based on a single-layer coplanar design.

In this paper, a tunable five-band terahertz absorber based on a graphene metasurface is proposed. It is a typical three-layer structure consisting of a bottom gold grounding layer, an intermediate polyimide dielectric layer, and a top patterned graphene layer. Five near-unity absorption could be realized, which could be characterized by polarization and angle sensitivity and wide-angle and flexible tunability. The results show that the peak absorbance reaches 96.4%, 99.4%, 99.8%, 98.4%, and 99.9% at 4.62 THz, 7.29 THz, 7.70 THz, 8.19 THz, and 8.93 THz, respectively. The resonance frequency of the absorber varies in direct proportion to the graphene's Fermi level. By adjusting the Fermi level of graphene, the absorber performance can be continuously adjusted within the working range, and the average absorption can be increased from 96.38% to 98.78%. By changing the angle of incidence, the absorber can be considered to have stable absorption performance within 0–65°, characterized by wide-angle incidence. Due to the excellent properties of the structure, such as high absorbance, strong tunability, and wide-angle absorption, it has a broad application prospect in the fields of terahertz sensing, nondestructive testing, imaging, stealth, and detectors.

## 2. Materials and Methods

Based on the design needs of a multi-band absorber, we designed a five-band absorber by combining two different shapes of split-ring structures based on the patterns of circular and square graphene rings. The designed five-band PA structure is shown in Figure 1, where Figure 1a,b show the side view of the structure and the top view of the patterned layer, respectively. The absorber system has a classical sandwich structure, where the bottom metal layer is separated from the top patterned layer by a layer of polyimide with a relative dielectric constant of 2.89 at a thickness of  $t_2 = 4 \mu\text{m}$ , and the patterned layer consists of two sets of different-sized graphene-based copper-coin-like resonators. Gold was chosen as the all-reflective metallic ground plane, whose conductivity is  $4.56 \times 10^7 \text{ S/m}$  with a thickness  $t_1 = 0.3 \mu\text{m}$ . The top view of the patterned graphene cell structure is shown in Figure 1b, and the specific optimized geometrical parameters are as follows:  $a = 2.0 \mu\text{m}$ ,  $b = 0.5 \mu\text{m}$ ,  $c = 1.2 \mu\text{m}$ ,  $r = 1.0 \mu\text{m}$ ,  $d = 0.15 \mu\text{m}$ , and  $\delta = 0.15 \mu\text{m}$ . The period of the unit cell in the  $x$  and  $y$  directions is  $P = 4 \mu\text{m}$ .

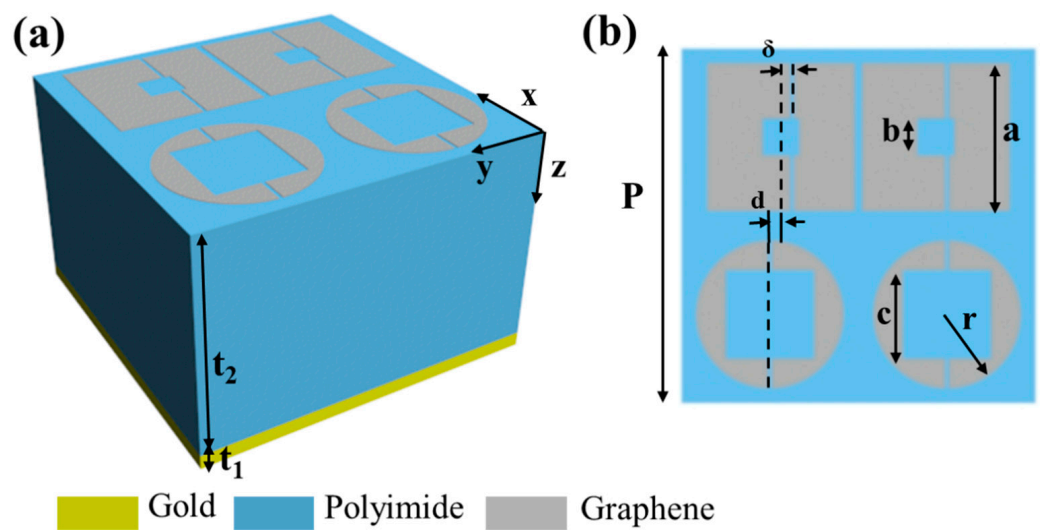


**Figure 1.** Schematic of (a) three-dimensional structure and (b) top view of the proposed metamaterial absorber. The structural parameters are set as follows:  $P = 4 \mu\text{m}$ ,  $t_1 = 0.3 \mu\text{m}$ ,  $t_2 = 4 \mu\text{m}$ ,  $a = 2.0 \mu\text{m}$ ,  $b = 0.5 \mu\text{m}$ ,  $c = 1.2 \mu\text{m}$ ,  $r = 1.0 \mu\text{m}$ ,  $d = 0.15 \mu\text{m}$ ,  $\delta = 0.15 \mu\text{m}$ .

The surface dielectric constant of graphene can be expressed as follows [53,54]:

$$\epsilon = 1 + i \frac{\sigma_{gra} Z_0}{k_0 d} \quad , \quad (1)$$

where the thickness of graphene is 0.334 nm, the free space impedance is  $Z_0 = 377 \text{ ohm}$ ,  $k_0$  denotes the wave vector number of free space electromagnetic wave, and  $\sigma_{gra}$  denotes the surface conductivity of graphene. In the model, the surface conductivity of monolayer graphene can be described by Kubo's formula, which includes intraband and interband terms [55,56]:

$$\sigma_{gra} = \sigma_{intra} + \sigma_{inter} \quad , \quad (2)$$

$$\sigma_{intra} = \frac{2e^2 k_B T}{\pi \hbar^2} \frac{i}{\omega + i/\tau} \ln \left[ 2 \cosh \left( \frac{E_f}{2k_B T} \right) \right] \quad , \quad (3)$$

$$\sigma_{inter} = \frac{e^2}{4\hbar^2} \left[ \frac{1}{2} + \frac{1}{\pi} \arctan \left( \frac{\hbar\omega - 2E_f}{2k_B T} \right) - \frac{i}{2\pi} \ln \frac{(\hbar\omega + 2E_f)^2}{(\hbar\omega - 2E_f)^2 + 4(k_B T)^2} \right] \quad , \quad (4)$$

where  $e$ ,  $T$ ,  $k_B$ , and  $\hbar$  are the charge of the electron, the absolute temperature ( $T = 300 \text{ K}$ ), Boltzmann's constant, and the approximate Planck's constant, respectively, and  $\omega$ ,  $\tau$ , and

$E_f$  are the angular frequency, the electron–phonon relaxation time, and the Fermi level, respectively. At a room temperature of 300 K,  $\hbar\omega \ll 2E_f$  within the terahertz frequency according to the Pauli exclusion principle. Intraband leaps in the terahertz region dominate compared to interband leaps. Therefore, the above equations can be simplified to a Drude-like form [57–59]:

$$\sigma_{gra} = \frac{e^2 E_f}{\pi \hbar^2} \frac{i}{\omega + i/\tau} \tag{5}$$

In the following study, the Fermi level is set as 1.2 eV, and the electron–phonon relaxation time is 1 ps. The absorption properties and physical mechanisms of this absorbing system are investigated in detail using the COMSOL Multiphysics 6.1 software based on the finite element method. The periodic boundary conditions are set in both  $x$ -axis and  $y$ -axis directions, and Floquet ports are assigned in the direction perpendicular to the graphene plane. In addition, the incident light source is a plane wave, incident in the  $x$  direction.

### 3. Results and Discussion

The absorption curve of the five-band metamaterial absorber is given in Figure 2. The absorption rate can be expressed as  $A(\omega) = 1 - R(\omega) - T(\omega) = 1 - |S_{11}|^2 - |S_{21}|^2$ , where  $A(\omega)$  denotes the absorptivity,  $S_{11}$ ,  $S_{21}$  are the scattering coefficients, the reflectivity is  $R(\omega) = |S_{11}|^2$ , and the transmittance is  $T(\omega) = |S_{21}|^2$ . In the terahertz range, the thickness of the gold is much larger than the skin depth. It can be approximated that  $T(\omega) = 0$ , so the absorptivity can be simplified to  $A(\omega) = 1 - |S_{11}|^2$ . The reflection is highly dependent on the impedance, and when the impedance is adjusted to match perfectly with free space, the incident wave can be absorbed significantly. From the impedance matching principle, the absorption rate can be expressed as follows [60–62]:

$$A(\omega) = 1 - R(\omega) = 1 - \left| \frac{Z - Z_0}{Z + Z_0} \right|^2 = 1 - \left| \frac{Z_r - 1}{Z_r + 1} \right|^2 \tag{6}$$

where  $Z$  and  $Z_0$  are the effective impedance of the absorber and free space, respectively, and the relative impedance of the absorber can be calculated by parametric inversion [63]:

$$Z_r = \sqrt{\frac{(1 + S_{11})^2 - S_{21}^2}{(1 - S_{11})^2 - S_{21}^2}} \tag{7}$$

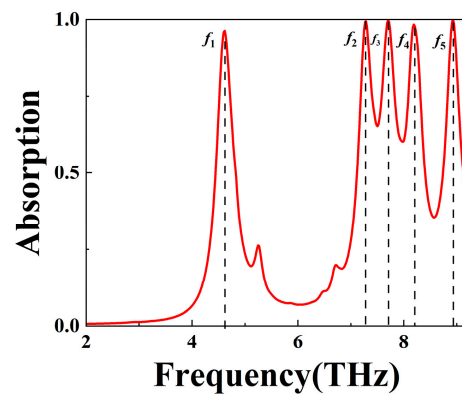


**Figure 2.** Absorption spectra of designed five-band terahertz absorber. The peak absorbance reached 96.4%, 99.4%, 99.8%, 98.4%, and 99.9% at  $f_1 = 4.62$  THz,  $f_2 = 7.29$  THz,  $f_3 = 7.70$  THz,  $f_4 = 8.19$  THz, and  $f_5 = 8.93$  THz, respectively.

The reflection coefficient is minimized when the absorber equivalent impedance matches the free space impedance. From the given design parameters, perfect absorption up to 96.4%, 99.4%, 99.8%, 98.4%, and 99.9% is achieved at five discrete points (labeled as

$f_1, f_2, f_3, f_4,$  and  $f_5$ ) at 4.62 THz, 7.29 THz, 7.70 THz, 8.19 THz, and 8.93 THz, respectively. Figure 3 shows the relative impedance of the absorber at the operating frequencies. The relative impedance of the absorber is highly matched to free space at five absorption frequencies, with the real part close to 1 and the imaginary part close to 0.

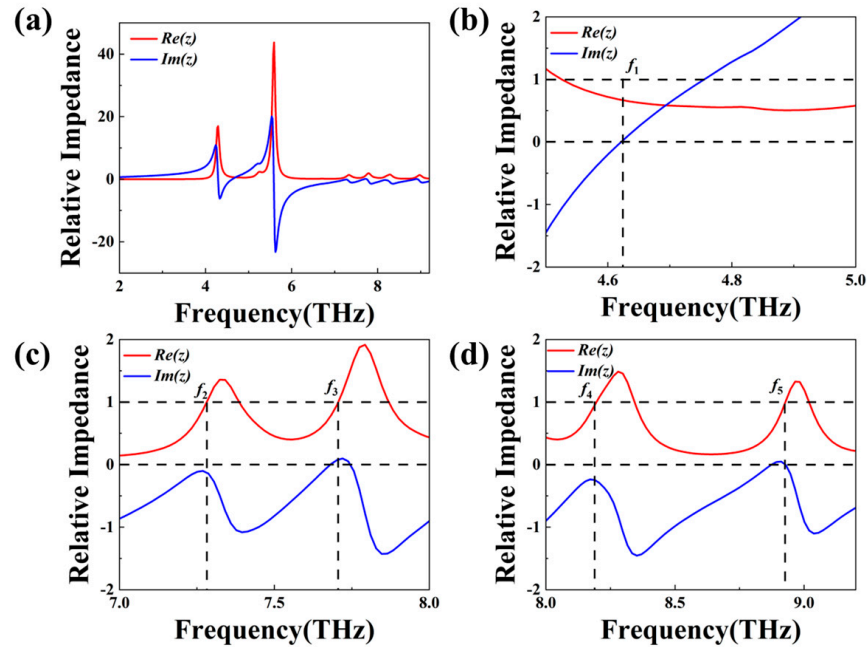


**Figure 3.** The relative impedance of (a) the absorber, and the relative impedance at (b–d)  $f_1 = 4.62$  THz,  $f_2 = 7.29$  THz,  $f_3 = 7.70$  THz,  $f_4 = 8.19$  THz, and  $f_5 = 8.93$  THz.

In order to further elaborate the absorption mechanism of five-band high absorption, the electric field distributions,  $E_z$ , and the current density distributions corresponding to the five absorption peaks of the metamaterial absorber are given in Figures 4 and 5. For  $f_1 = 4.62$  THz, consider the square resonator as an inductor, L, and the opening as a capacitor, C. According to the principle of equivalent circuit, the induced charges are generated by an electromagnetic wave at an incidence converge at the slit to form an electric field. Due to the narrow spatial position at the square ring slit, the movement of the charge forms a displacement current. As shown in Figure 4c, at this location, the current forms a loop on the graphene surface, producing an LC resonance mode. We can find that the electric field is partially concentrated at the top and bottom of the lower side of the copper-coin-like resonator due to the excitation of the surface plasmon excitations. It can be assumed that the high absorption at  $f_1 = 4.62$  THz is produced by the combined effect of two different sizes of copper-coin-like resonators. For the absorption peak at  $f_2 = 7.29$  THz, the electric field is mainly concentrated above the left-side square ring resonance cavity splits and below the right-side square ring resonance cavity splits, while some electric field distributions of relatively low intensity also exist around the outer ring. The coupling between the surface electronic oscillations of graphene and the incident electromagnetic wave enhances the localized electric field at the cleavage. This localization of the electromagnetic field leads to the localization of the optical field, which significantly enhances the absorption of light. Figure 4b,e represent the distribution of the z-component of the electric field in the corresponding modes, both of which are in good agreement with the distribution of the electric field, corroborating the analysis.

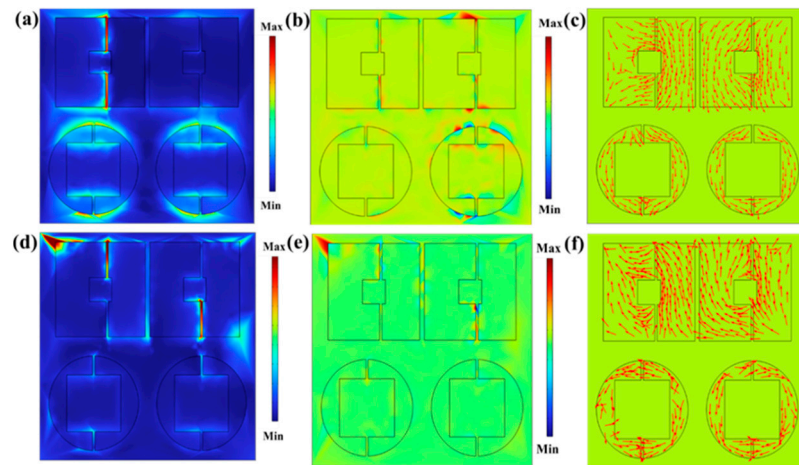


**Figure 4.** The electric field distributions of the absorber at (a) 4.62 THz and (d) 7.29 THz, while (b) and (e) show the respective  $E_z$  maps. The current density distributions at (c) 4.62 THz and (f) 7.29 THz.

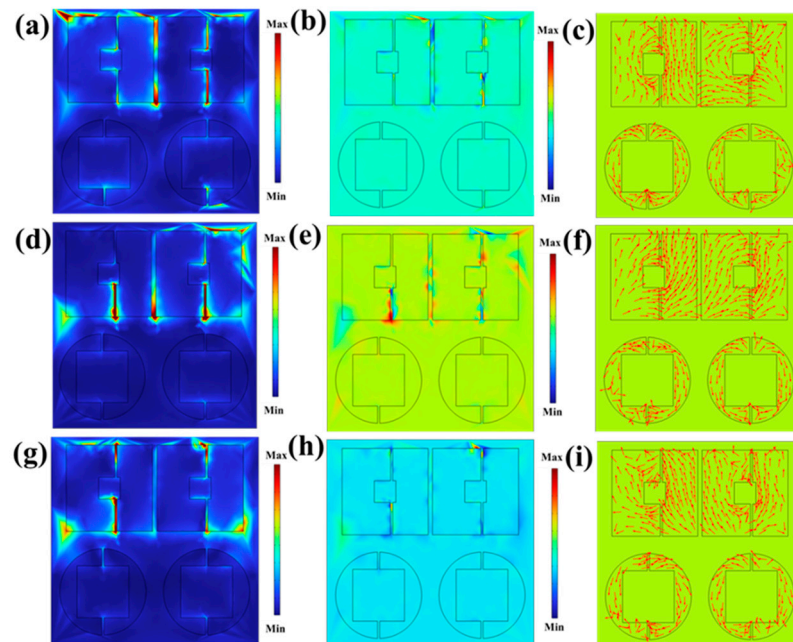


**Figure 5.** The electric field distributions of the absorber at (a) 7.70 THz, (d) 8.19 THz, and (g) 8.93 THz; (b,e,h) are the respective  $E_z$  maps. The current density distributions at (c) 7.70 THz, (f) 8.19 THz, and (i) 8.93 THz.

At  $f_3 = 7.70$  THz, the electric field is mainly concentrated at the cleavage of the right square ring, where the graphene surface couples with the magnetic field to enhance the absorption effect. The spacing between the upper two resonators is pulled in compared to the lower two resonators, and there is a strong coupling effect, and the electromagnetic wave induces a localized surface plasma resonance at this slit. At the same time, the uppermost edge of the outer ring is also accompanied by an electric field distribution, which is conducive to increased absorption. At  $f_4 = 8.19$  THz, the electric field is mainly concentrated in the lower part of the square ring resonator cavity at the slit. Figure 5e shows the  $E_z$  distribution at  $f_4 = 8.19$  THz. For the lower side opening of the left square ring resonator, the positive charges are concentrated at the left end, and the negative charges are concentrated at the right end, forming a dipole resonance. Similarly, a dipole resonance is formed on the right-side square ring resonator, but with opposite polarity to the left side. For the peak at  $f_5 = 8.93$  THz, the absorption pattern is similar to the peak at  $f_3 = 7.70$  THz,

and the electric field is concentrated at the slit of the square annular resonant cavity. The electromagnetic wave induces localized surface plasmon resonance at the above location, which significantly enhances the absorption effect. The surface currents in Figure 5e,f,i also correspond well with the electric field, and the currents are mainly concentrated at the slit or in the narrow region of the space between the two resonators.

Figure 6 illustrates the effect of the variation in the geometrical parameters of the device on the absorption effect. As shown in Figure 6a, when the edge length  $a$  increases, the frequency of the  $f_1$  undergoes a slight redshift, and the  $f_2$ – $f_5$  absorption intensities undergo significant changes. With the increase in  $a$ , the effective area of graphene increases, the distance between the two sub-resonant cavities above gradually draws closer, the mutual coupling interaction is enhanced, and the absorption capacity increases. However, after increasing to a certain value, an interaction that is too strong causes the absorption rate to decrease. Figure 6b shows the absorption spectra under different parameters above the hollow square sheet  $b$ . With the change in  $b$ , the overall frequency range is slightly redshifted and then significantly blue-shifted, and there is a tendency to cleave into two peaks at  $f_1$ , and the overall absorption quality increases and then weakens. With an increasing  $b$  value, the internal arrangement of graphene becomes denser, and the increase in surface plasmon exciton polarizers leads to an increase in absorbance. However, after reaching the peak, the resonance peaks excited between different regions interfere with each other, leading to a decrease in the absorption rate. Similarly, the change in the absorption pattern of parameter  $c$  is similar to that of  $b$ . The effect of the parameter  $r$  of the copper-coin-shaped resonator on the absorption rate is similar to that of  $a$ , which can be attributed to the increase in the effective area of graphene and the generation of interactions.

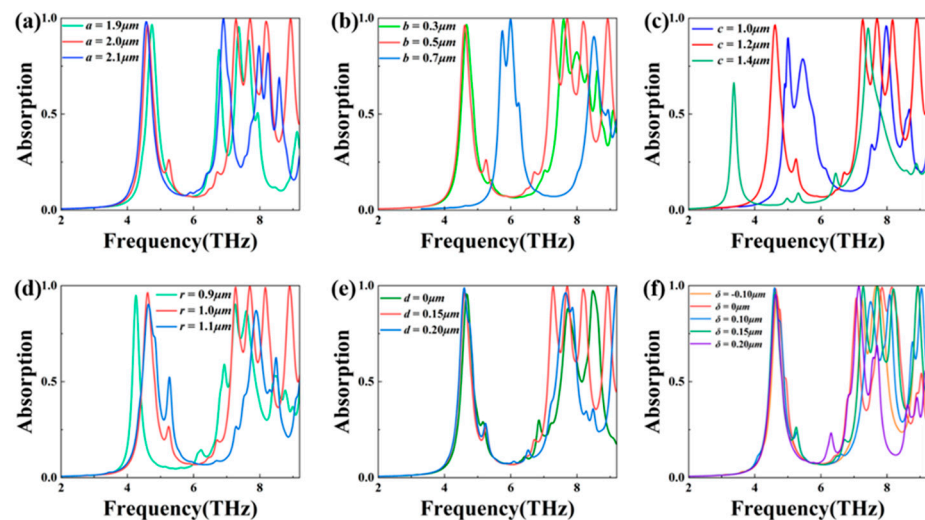


**Figure 6.** Absorption spectra with different values of (a) parameter  $a$ , (b) parameter  $b$ , (c) parameter  $c$ , (d) parameter  $r$ , (e) parameter  $d$ , and (f) parameter  $r$ . The other default parameters are the same as those illustrated in Figure 1.

Based on the need for a compact design, in the process of translating each of the upper two square rings to the center axis, we found interesting phenomena. According to the absorption curves and trends, the number of absorption peaks mutates from three peaks to five peaks. When  $d = 0 \mu\text{m}$ , the overall pattern is horizontally symmetric about the central axis, at which time there are three absorption peaks, but the center front absorption quality is low. With the increase in  $d$ , the upper two square rings are gradually close to each other, and the coupling between them increases significantly, improving the absorption quality. After reaching the peak, the operating band undergoes a significant blue shift. In order to improve the overall absorption performance of the absorber, based on the original design, the slits are skeletonized at different locations to form splits. From the absorption mechanism analyzed earlier, the absorption strength depends largely on the

plasma resonance at the slits. When  $\delta = 0 \mu\text{m}$ , both splits are located at the centrosymmetric position of the associated geometrical structure, but at this time, the absorption mode is three-peaked and there are oscillating peaks with poor absorption quality. With the change in the position of  $\delta$ , the absorption intensity reaches the optimal value at  $\delta = 0.15 \mu\text{m}$ . The thickness of the dielectric layer has a significant effect on the absorption profile.

The Fermi level of graphene can be continuously tuned by applying a bias voltage or chemical doping on the graphene surface. The absorption spectra at different Fermi levels are shown in Figure 7a. The theoretical calculations show that the five absorption frequency points exhibit an obvious blue shift with the increase in the Fermi level, the absorption intensity at  $f_1$  decreases, and the absorption intensities at  $f_2$ – $f_5$  increase and then decrease. Meanwhile, to clearly illustrate the frequency tunability of the designed graphene metamaterial absorber, we plotted the absorptivity as a function of the Fermi levels and resonance frequencies, as shown in Figure 7b. The relationship between the Fermi level and the graphene-based absorber resonance frequency can be expressed as follows [64]:

$$f \propto \sqrt{\frac{\alpha_0 E_f}{2\pi^2 \hbar v L}} \tag{8}$$

where  $\alpha_0 = \frac{e^2}{\hbar}$  is the structural constant of graphene,  $L$  is the length of the graphene strip, and  $v$  is the speed of light in a vacuum. Based on the dynamic tunable properties of graphene, we can flexibly adjust the absorption intensity and operating frequency of the absorber by changing the Fermi level of graphene without changing the geometrical parameters of the absorber. In addition, as shown in Figure 7c, changes in the thickness of the dielectric layer bring about significant changes in the number of absorption peaks. A dielectric layer that is too thin can cause electromagnetic waves that penetrate the entire structure, while a dielectric layer that is too thick can cause multiple oscillations of electromagnetic waves in the cavity. Thus,  $t_2$  reaches the optimum value at  $4 \mu\text{m}$ .

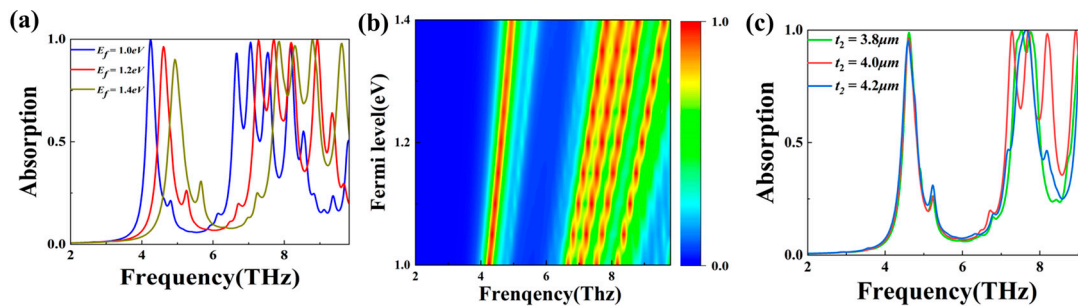


**Figure 7.** (a) Absorption spectra and (b) frequency shifts at different Fermi levels. The absorption spectra with (c) different dielectric layer thickness  $t_2$ .

Combined with practical engineering applications, we need to consider the incident wave under oblique incidence. In the COMSOL Multiphysics 6.1 software, we parameterized the incidence elevation angle and finally obtained the absorption spectra at different incidence angles, as shown in Figure 8. As the incident angle increases in  $10^\circ$  steps, different frequency points have different angular dependencies. The absorption performance of  $f_1$  is stable with the increase in the incidence angle, and the intensity remains unchanged between  $0$  and  $70^\circ$ . The  $f_2$  and  $f_3$  values decrease in absorption intensity at the absorption angle of  $65^\circ$ , and the position of the frequency point is almost unchanged. The  $f_4$  and  $f_5$  values undergo a significant decrease in intensity at the incidence angle of more than  $60^\circ$ , and the frequency point is shifted slightly in comparison with the center position. The results show that the absorber can maintain the absorption stability under a wide incidence angle of  $0$ – $65^\circ$  and exhibits wide-angle incidence characteristics.

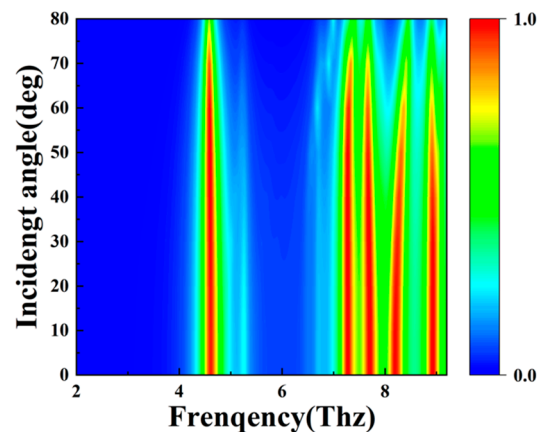


**Figure 8.** Absorption as a function of frequency and angle of incidence.

#### 4. Conclusions

In summary, a multi-band tunable terahertz perfect absorber based on a graphene metasurface, which has a typical three-layer sandwich structure, is proposed in this paper. The numerical simulation results confirm the existence of five perfect absorption peaks in the terahertz operating range of this structure, which can realize high-quality absorption with an average absorption rate of 98.78%. By precisely adjusting the structural parameters of the patterned graphene layer and the thickness of the dielectric layer, the number and intensity of absorption peaks can be adjusted to the desired values. The numerical results show that the absorber has stable absorption performance in the range of 0–65° in the incidence angle with wide-angle incidence. When the Fermi level is adjusted in the range of 1.0–1.4 eV, the average peak absorption increases from 96.38% to 98.78%. Additionally, we can realize the continuous tuning of the absorption performance in a wide frequency range by changing the Fermi level of the graphene. Given the excellent properties of the designed absorber, such as high absorption, dynamic tuning, and wide incidence angle, our design has potential applications in the fields of nondestructive testing, imaging, communication, sensing, and detectors.

**Author Contributions:** J.W. created the models, conducted the simulation, discussed the results, analyzed the data, and wrote the original manuscript. X.Q. discussed the results and analyzed the data. Q.Z. discussed the results and analyzed the data. G.D. discussed the results. B.-X.W. supervised this project, provided the original idea and funding, discussed the results, analyzed the data, and revised the manuscript. All authors have read and agreed to the published version of the manuscript.

**Funding:** This research was funded by the National Natural Science Foundation of China (62105128), the China Postdoctoral Science Foundation (2023M741401), the China Scholarship Council (202106795002), Key Research and Development Program of Zhejiang Province (2023C04015); Key Research and Development Program of Huzhou (2022ZD2029), the Key Lab of Modern Optical Technologies of Education Ministry of China, Soochow University, and the Jiangsu Province Training Program of Innovation and Entrepreneurship for Undergraduates (202310295138Y).

**Institutional Review Board Statement:** Not applicable.

**Informed Consent Statement:** Not applicable.

**Data Availability Statement:** The data and material that support the findings of this study are available from the corresponding author upon reasonable request.

**Acknowledgments:** The authors thank the reviewers and editors for their selfless efforts and pertinent suggestions.

**Conflicts of Interest:** The authors declare no conflicts of interest.

## References

1. Huang, Y.; Shen, Y.; Wang, J. From Terahertz Imaging to Terahertz Wireless Communications. *Engineering* **2023**, *22*, 106–124. [[CrossRef](#)]
2. Roh, Y.; Lee, S.-H.; Kwak, J.; Song, H.S.; Shin, S.; Kim, Y.K.; Wu, J.W.; Ju, B.-K.; Kang, B.; Seo, M. Terahertz imaging with metamaterials for biological applications. *Sens. Actuators B Chem.* **2022**, *352*, 130993. [[CrossRef](#)]
3. Yang, S.; Ding, L.; Wang, S.; Du, C.; Feng, L.; Qiu, H.; Zhang, C.; Wu, J.; Fan, K.; Jin, B.; et al. Studying Oral Tissue via Real-Time High-Resolution Terahertz Spectroscopic Imaging. *Phys. Rev. Appl.* **2023**, *19*, 034033. [[CrossRef](#)]
4. Serghiou, D.; Khalily, M.; Brown, T.W.C.; Tafazolli, R. Terahertz Channel Propagation Phenomena, Measurement Techniques and Modeling for 6G Wireless Communication Applications: A Survey, Open Challenges and Future Research Directions. *IEEE Commun. Surv. Tutor.* **2022**, *24*, 1957–1996. [[CrossRef](#)]
5. Xiao, S.; Wang, T.; Liu, T.; Zhou, C.; Jiang, X.; Zhang, J. Active metamaterials and metadevices: A review. *J. Phys. D Appl. Phys.* **2020**, *53*, 503002. [[CrossRef](#)]
6. Szabó, Z.; Fűzi, J. Equivalence of Magnetic Metamaterials and Composites in the View of Effective Medium Theories. *IEEE Trans. Magn.* **2014**, *50*, 1–4. [[CrossRef](#)]
7. Park, C.M.; Lee, S.H. Zero-reflection acoustic metamaterial with a negative refractive index. *Sci. Rep.* **2019**, *9*, 3372. [[CrossRef](#)] [[PubMed](#)]
8. Padilla, W.J.; Basov, D.N.; Smith, D.R. Negative refractive index metamaterials. *Mater. Today* **2006**, *9*, 28–35. [[CrossRef](#)]
9. Abdulkarim, Y.I.; Özkan Alkurt, F.; Awl, H.N.; Muhammadsharif, F.F.; Bakır, M.; Dalgac, S.; Karaaslan, M.; Luo, H. An ultrathin and dual band metamaterial perfect absorber based on ZnSe for the polarization-independent in terahertz range. *Results Phys.* **2021**, *26*, 104344. [[CrossRef](#)]
10. Jen, Y.-J.; Liu, W.-C.; Chen, T.-K.; Lin, S.-w.; Jhang, Y.-C. Design and deposition of a metal-like and admittance-matching metamaterial as an ultra-thin perfect absorber. *Sci. Rep.* **2017**, *7*, 3076. [[CrossRef](#)]
11. Zhai, S.L.; Zhao, X.P.; Liu, S.; Shen, F.L.; Li, L.L.; Luo, C.R. Inverse Doppler Effects in Broadband Acoustic Metamaterials. *Sci. Rep.* **2016**, *6*, 32388. [[CrossRef](#)]
12. Shi, X.; Lin, X.; Kaminer, I.; Gao, F.; Yang, Z.; Joannopoulos, J.D.; Soljačić, M.; Zhang, B. Superlight inverse Doppler effect. *Nat. Phys.* **2018**, *14*, 1001–1005. [[CrossRef](#)]
13. Luo, W.; Wang, X.; Chen, X.; Zheng, S.; Zhao, S.; Wen, Y.; Li, L.; Zhou, J. Perfect absorption based on a ceramic anapole metamaterial. *Mater. Horiz.* **2023**, *10*, 1769–1779. [[CrossRef](#)]
14. Zhao, X.; Yuan, C.; Zhu, L.; Yao, J. Graphene-based tunable terahertz plasmon-induced transparency metamaterial. *Nanoscale* **2016**, *8*, 15273–15280. [[CrossRef](#)]
15. Chen, S.; Zeng, L.; Li, J.; Weng, J.; Li, J.; Guo, Z.; Xu, P.; Liu, W.; Yang, J.; Qin, Y.; et al. Tunable plasmon-induced transparency with coupled L-shape graphene metamaterial. *Results Phys.* **2022**, *38*, 105537. [[CrossRef](#)]
16. Chen, T.; Yu, D.; Wu, B.; Xia, B. Weak Signals Detection by Acoustic Metamaterials-Based Sensor. *IEEE Sens. J.* **2021**, *21*, 16815–16825. [[CrossRef](#)]
17. Cao, P.; Wu, Y.; Wang, Z.; Li, Y.; Zhang, J.; Liu, Q.; Cheng, L.; Niu, T. Tunable Dual-Band Ultrasensitive Stereo Metamaterial Terahertz Sensor. *IEEE Access* **2020**, *8*, 219525–219533. [[CrossRef](#)]
18. Landy, N.I.; Sajuyigbe, S.; Mock, J.J.; Smith, D.R.; Padilla, W.J. Perfect Metamaterial Absorber. *Phys. Rev. Lett.* **2008**, *100*, 207402. [[CrossRef](#)] [[PubMed](#)]
19. Sayed, S.I.; Mahmoud, K.R.; Mubarak, R.I. Design and optimization of broadband metamaterial absorber based on manganese for visible applications. *Sci. Rep.* **2023**, *13*, 11937. [[CrossRef](#)]
20. Nandakumar, S.; Trabelsi, Y.; Vasudevan, B.; Gunasekaran, S. MXene fractal-based dual-band metamaterial absorber in the visible and near-infrared regime. *Opt. Quantum Electron.* **2023**, *55*, 992. [[CrossRef](#)]
21. Zhang, Y.; Lv, J.; Que, L.; Mi, G.; Zhou, Y.; Jiang, Y. A visible-infrared double band photodetector absorber. *Results Phys.* **2020**, *18*, 103283. [[CrossRef](#)]
22. Hu, D.; Wang, H.y.; Zhu, Q.f. Design of Six-Band Terahertz Perfect Absorber Using a Simple U-Shaped Closed-Ring Resonator. *IEEE Photonics J.* **2016**, *8*, 1–8. [[CrossRef](#)]
23. Lou, P.; He, Y.; Zhu, H.; Zhang, X.; Hu, L.; Wang, B.-X. Multiple-band terahertz perfect light absorbers enabled by using multiple metallic bars. *Phys. Scr.* **2021**, *96*, 055502. [[CrossRef](#)]
24. Wen, Q.-Y.; Zhang, H.-W.; Xie, Y.-S.; Yang, Q.-H.; Liu, Y.-L. Dual band terahertz metamaterial absorber: Design, fabrication, and characterization. *Appl. Phys. Lett.* **2009**, *95*, 241111. [[CrossRef](#)]
25. Wang, J.; Lang, T.; Hong, Z.; Xiao, M.; Yu, J. Design and Fabrication of a Triple-Band Terahertz Metamaterial Absorber. *Nanomaterials* **2021**, *11*, 1110. [[CrossRef](#)] [[PubMed](#)]
26. Fu, G.; Liu, X.; Huang, Z.; Chen, J.; Liu, Z. Metallic Metasurfaces for Light Absorbers. *IEEE Photonics Technol. Lett.* **2017**, *29*, 47–50. [[CrossRef](#)]
27. Huang, S.; Xie, Z.; Chen, W.; Lei, J.; Wang, F.; Liu, K.; Li, L. Metasurface with multi-sized structure for multi-band coherent perfect absorption. *Opt. Express* **2018**, *26*, 7066–7078. [[CrossRef](#)]
28. Niu, T.; Qiu, B.; Zhang, Y.; Hirakawa, K. Control of absorption properties of ultra-thin metal–insulator–metal metamaterial terahertz absorbers. *Jpn. J. Appl. Phys.* **2020**, *59*, 120904. [[CrossRef](#)]

29. Zhou, Y.; Xia, H.; Zhang, L.; Zhao, Y.; Xie, W. Temperature insensitive ultra-broadband THz metamaterial absorber based on metal square ring resonators. *Results Phys.* **2021**, *22*, 103915. [[CrossRef](#)]
30. Tang, H.; Menabde, S.G.; Anwar, T.; Kim, J.; Jang, M.S.; Tagliabue, G. Photo-modulated optical and electrical properties of graphene. *Nanophotonics* **2022**, *11*, 917–940. [[CrossRef](#)]
31. Chang, K.; Li, Z.; Gu, Y.; Liu, K.; Chen, K. Graphene-integrated waveguides: Properties, preparation, and applications. *Nano Res.* **2022**, *15*, 9704–9726. [[CrossRef](#)]
32. Pumera, M.; Sofer, Z. Towards stoichiometric analogues of graphene: Graphane, fluorographene, graphol, graphene acid and others. *Chem. Soc. Rev.* **2017**, *46*, 4450–4463. [[CrossRef](#)]
33. Armaković, S.; Armaković, S.J. Investigation of boron modified graphene nanostructures; optoelectronic properties of graphene nanoparticles and transport properties of graphene nanosheets. *J. Phys. Chem. Solids* **2016**, *98*, 156–166. [[CrossRef](#)]
34. Lv, Y.; Li, H.; Coileáin, C.Ó.; Zhang, D.; Heng, C.; Chang, C.-R.; Hung, K.M.; Cheng, H.H.; Wu, H.-C. Photoelectrical properties of graphene/doped GeSn vertical heterostructures. *RSC Adv.* **2020**, *10*, 20921–20927. [[CrossRef](#)] [[PubMed](#)]
35. Miao, W.; Wang, L.; Mu, X.; Wang, J. The magical photoelectric and optoelectronic properties of graphene nanoribbons and their applications. *J. Mater. Chem. C* **2021**, *9*, 13600–13616. [[CrossRef](#)]
36. Tiutiunnyk, A.; Duque, C.A.; Caro-Lopera, F.J.; Mora-Ramos, M.E.; Correa, J.D. Opto-electronic properties of twisted bilayer graphene quantum dots. *Phys. E Low-Dimens. Syst. Nanostructures* **2019**, *112*, 36–48. [[CrossRef](#)]
37. Wang, J.; Song, J.; Mu, X.; Sun, M. Optoelectronic and photoelectric properties and applications of graphene-based nanostructures. *Mater. Today Phys.* **2020**, *13*, 100196. [[CrossRef](#)]
38. Wang, J.; Yang, H.; Yang, P. Photoelectric properties of 2D ZnO, graphene, silicene materials and their heterostructures. *Compos. Part B Eng.* **2022**, *233*, 109645. [[CrossRef](#)]
39. Wirth-Lima, A.J.; Alves-Sousa, P.P.; Bezerra-Fraga, W. Graphene's photonic and optoelectronic properties—A review. *Chin. Phys. B* **2020**, *29*, 037801. [[CrossRef](#)]
40. Chen, D.; Yang, J.; Huang, J.; Zhang, Z.; Xie, W.; Jiang, X.; He, X.; Han, Y.; Zhang, Z.; Yu, Y. Continuously tunable metasurfaces controlled by single electrode uniform bias-voltage based on nonuniform periodic rectangular graphene arrays. *Opt. Express* **2020**, *28*, 29306–29317. [[CrossRef](#)]
41. Liu, W.; Song, Z.; Wang, W. A high-performance broadband terahertz absorber based on multilayer graphene squares. *Phys. Scr.* **2021**, *96*, 055504. [[CrossRef](#)]
42. Ma, L.; Wang, Z.; Han, X. A Transparent Tunable Broadband Microwave Absorber Based on Multi-layer Structure by Patterned Graphene. *J. Phys. Conf. Ser.* **2023**, *2434*, 012001. [[CrossRef](#)]
43. Zhai, Z.; Zhang, L.; Li, X.; Xiao, S. Tunable terahertz broadband absorber based on a composite structure of graphene multilayer and silicon strip array. *Opt. Commun.* **2019**, *431*, 199–202. [[CrossRef](#)]
44. Cai, Y.; Xu, K.-D. Tunable broadband terahertz absorber based on multilayer graphene-sandwiched plasmonic structure. *Opt. Express* **2018**, *26*, 31693–31705. [[CrossRef](#)]
45. Yue, J.; Shang, X.-j.; Zhai, X.; Wang, L.-l. Numerical Investigation of a Tunable Fano-Like Resonance in the Hybrid Construction Between Graphene Nanorings and Graphene Grating. *Plasmonics* **2017**, *12*, 523–528. [[CrossRef](#)]
46. Pan, Q.; Zhang, G.; Pan, R.; Zhang, J.; Shuai, Y.; Tan, H. Tunable absorption as multi-wavelength at infrared on graphene/hBN/Al grating structure. *Opt. Express* **2018**, *26*, 18230–18237. [[CrossRef](#)] [[PubMed](#)]
47. Patel, S.K.; Ladumor, M.; Sorathiya, V.; Guo, T. Graphene based tunable grating structure. *Mater. Res. Express* **2019**, *6*, 025602. [[CrossRef](#)]
48. Wu, J. Enhancement of Absorption in Graphene Strips with Cascaded Grating Structures. *IEEE Photonics Technol. Lett.* **2016**, *28*, 1332–1335. [[CrossRef](#)]
49. Liu, L.; Liu, W.; Song, Z. Ultra-broadband terahertz absorber based on a multilayer graphene metamaterial. *J. Appl. Phys.* **2020**, *128*, 093104. [[CrossRef](#)]
50. Gong, D.; Mei, J.; Li, N.; Shi, Y. Tunable metamaterial absorber based on VO<sub>2</sub>-graphene. *Mater. Res. Express* **2022**, *9*, 115803. [[CrossRef](#)]
51. Liu, Y.; Zhong, R.; Huang, J.; Lv, Y.; Han, C.; Liu, S. Independently tunable multi-band and ultra-wide-band absorbers based on multilayer metal-graphene metamaterials. *Opt. Express* **2019**, *27*, 7393–7404. [[CrossRef](#)] [[PubMed](#)]
52. Shoghi Badr, N.; Moradi, G. Design and analysis of graphene-based THz absorber using multi-layer structure based on increasing profile for conductivity of the graphene layers. *Optik* **2019**, *198*, 163239. [[CrossRef](#)]
53. Wang, B.; Zeng, Q.; Xiao, S.; Xu, C.; Xiong, L.; Lv, H.; Du, J.; Yu, H. Low-power, ultrafast, and dynamic all-optical tunable plasmon induced transparency in two stub resonators side-coupled with a plasmonic waveguide system. *J. Phys. D Appl. Phys.* **2017**, *50*, 455107. [[CrossRef](#)]
54. Liu, C.; Su, W.; Liu, Q.; Lu, X.; Wang, F.; Sun, T.; Chu, P.K. Symmetrical dual D-shape photonic crystal fibers for surface plasmon resonance sensing. *Opt. Express* **2018**, *26*, 9039–9049. [[CrossRef](#)] [[PubMed](#)]
55. Demetriou, G.; Bookey, H.T.; Biancalana, F.; Abraham, E.; Wang, Y.; Ji, W.; Kar, A.K. Nonlinear optical properties of multilayer graphene in the infrared. *Opt. Express* **2016**, *24*, 13033–13043. [[CrossRef](#)]
56. Hanson, G.W. Dyadic Green's functions and guided surface waves for a surface conductivity model of graphene. *J. Appl. Phys.* **2008**, *103*, 064302. [[CrossRef](#)]

57. Chen, P.; Tang, M.; Liu, A.; Hu, Y.; Li, L.; Chen, W.; Su, Y.; Huang, Y.; Zheng, J.; Liu, K.; et al. Polarization-sensitive tunable multi-band terahertz absorber based on single-layered graphene rings. *J. Opt. Soc. Am. B* **2021**, *38*, 3000–3008. [[CrossRef](#)]
58. Mou, N.; Sun, S.; Dong, H.; Dong, S.; He, Q.; Zhou, L.; Zhang, L. Hybridization-induced broadband terahertz wave absorption with graphene metasurfaces. *Opt. Express* **2018**, *26*, 11728–11736. [[CrossRef](#)]
59. Wu, Z.; Xu, B.; Yan, M.; Wu, B.; Cheng, P.; Sun, Z. Tunable terahertz perfect absorber with a graphene-based double split-ring structure. *Opt. Mater. Express* **2021**, *11*, 73–79. [[CrossRef](#)]
60. Biabanifard, S. A graphene-based dual-band THz absorber design exploiting the impedance-matching concept. *J. Comput. Electron.* **2021**, *20*, 38–48. [[CrossRef](#)]
61. Mei, P.; Zhang, S.; Lin, X.Q.; Pedersen, G.F. A Triple-Band Absorber with Wide Absorption Bandwidths Using an Impedance Matching Theory. *IEEE Antennas Wirel. Propag. Lett.* **2019**, *18*, 521–525. [[CrossRef](#)]
62. Smith, D.R.; Vier, D.C.; Koschny, T.; Soukoulis, C.M. Electromagnetic parameter retrieval from inhomogeneous metamaterials. *Phys. Rev. E* **2005**, *71*, 036617. [[CrossRef](#)] [[PubMed](#)]
63. Li, H.; Xu, W.; Cui, Q.; Wang, Y.; Yu, J. Theoretical design of a reconfigurable broadband integrated metamaterial terahertz device. *Opt. Express* **2020**, *28*, 40060–40074. [[CrossRef](#)] [[PubMed](#)]
64. Cheng, H.; Chen, S.; Yu, P.; Duan, X.; Xie, B.; Tian, J. Dynamically tunable plasmonically induced transparency in periodically patterned graphene nanostrips. *Appl. Phys. Lett.* **2013**, *103*, 203112. [[CrossRef](#)]

**Disclaimer/Publisher’s Note:** The statements, opinions and data contained in all publications are solely those of the individual author(s) and contributor(s) and not of MDPI and/or the editor(s). MDPI and/or the editor(s) disclaim responsibility for any injury to people or property resulting from any ideas, methods, instructions or products referred to in the content.